TECHNISCHE MECHANIK
European Journal of Engineering Mechanics
Diamond Open Access
journal homepage: www.ovgu.de/techmech

Tech. Mech., Vol. 46, Is. 1, (2026), 1–11
Received: 21.10.2025
Accepted: 08.01.2026
Available online: 16.02.2026

An experimental study with high-speed PIV to characterize the laminar - turbulent transition in helically coiled reactors.

Conrad Müller*, Péter Kováts, Dominique Thévenin and Katharina Zähringer

Otto-von-Guericke-Universität Magdeburg, Laboratory of Fluid Dynamics and Technical Flows, Universitätsplatz 2, 39106 Magdeburg, Germany

Abstract: Helically coiled reactors (HCRs) are widely used in process engineering and biochemistry, especially in micro-reactor applications, to enhance heat and mass transfer. Their design promotes excellent radial mixing with minimal axial back-mixing. At moderate Reynolds numbers, characteristic Dean vortices form within HCRs. Increasing flow velocities lead to more complex vortex structures. The transition from laminar to turbulent flow significantly impacts reactor performance. Various experimental and numerical studies have attempted to characterize this transition, often using a critical Reynolds number based on the curvature ratio $\delta = d/D$. Although it is generally accepted that HCRs have higher critical Reynolds numbers than straight tubes, reported values differ widely, possibly due to variations in experimental setups and inlet conditions. We propose a novel experimental setup designed to minimize the influence of inlet and outlet conditions. Reynolds numbers from 460 to 9,650 were examined. Initial Laser Doppler Velocimetry (LDV) measurements reveal that velocity fluctuations are weaker near the inner wall and stronger near the outer wall. High-speed Particle Image Velocimetry (PIV) measurements corroborate these findings. Additionally, we demonstrate how inlet conditions influence the transition point and discuss different markers for the laminar-turbulent transition in HCRs through pseudo-3D visualizations, frequency analysis, and qualitative flow analysis.

Keywords: helically coiled reactor, LDV, PIV, transition, turbulence

Nomenclature

Roman symbols

$\dot{V}$	volume flow rate [L min^{-1}]
$\mathrm{Re} = \frac{\rho\, u_b\, d}{\mu}$	Reynolds number –
D	coil diameter [mm]
d	inner tube diameter [mm]
f	frequency [s^{-1}]
f_{rec}	recording frequency [s^{-1}]
n	refractive index –
Q	Q-criterion [s^{-2}]
Q^*	dimensionless Q-criterion –
u_a	axial velocity [m s^{-1}]
u_b	bulk flow velocity [m s^{-1}]
u_r	radial velocity [m s^{-1}]

Greek symbols

$\delta = d/D$	curvature ratio –
μ	dynamic viscosity [kg m^{-1} s^{-1}]
ρ	density [kg m^{-3}]

Abbreviations

FEP	Fluorethylenepropylene
FFT	Fast Fourier Transformation
HCR	Helically Coiled Reactor
LDV	Laser Doppler Velocimetry
PIV	Particle Image Velocimetry
PMMA	Polymethylmethacrylate

1 Introduction

Helically coiled reactors (HCRs) – also called simply helix reactors in what follows – have a wide usage in industrial applications as static mixers and for an efficient heat and mass transfer. New patented geometries (Mansour and Thévenin, 2023) rose interest in a deeper understanding of the flow dynamics in helix reactor geometries. The influence of geometrical parameters (Kockmann, 2020), curvature ratio (Hüttl and Friedrich, 2000), torsion (Xie, 1990), and pitch (Florit et al., 2021; Liu et al., 1994; Manlapaz and Churchill, 1980), as well as the resulting pressure drop (Ali, 2001; Das, 1996) and the impact on heat and mass transfer have been already well investigated. Laminar-turbulent transition in helically coiled reactors has been the subject of many investigations since very first studies done by Taylor (1929) and White (1929). However, the results of all those investigations reveal major inconsistencies. Additionally, a detailed visualization of the associated flow structures has never been proposed. Figure 1 shows the most important literature findings illustrating the very diverse predictions regarding transition in HCRs with the present findings of

* E-mail address: conrad.mueller@ovgu.de
doi: 10.24352/UB.OVGU-2026-002

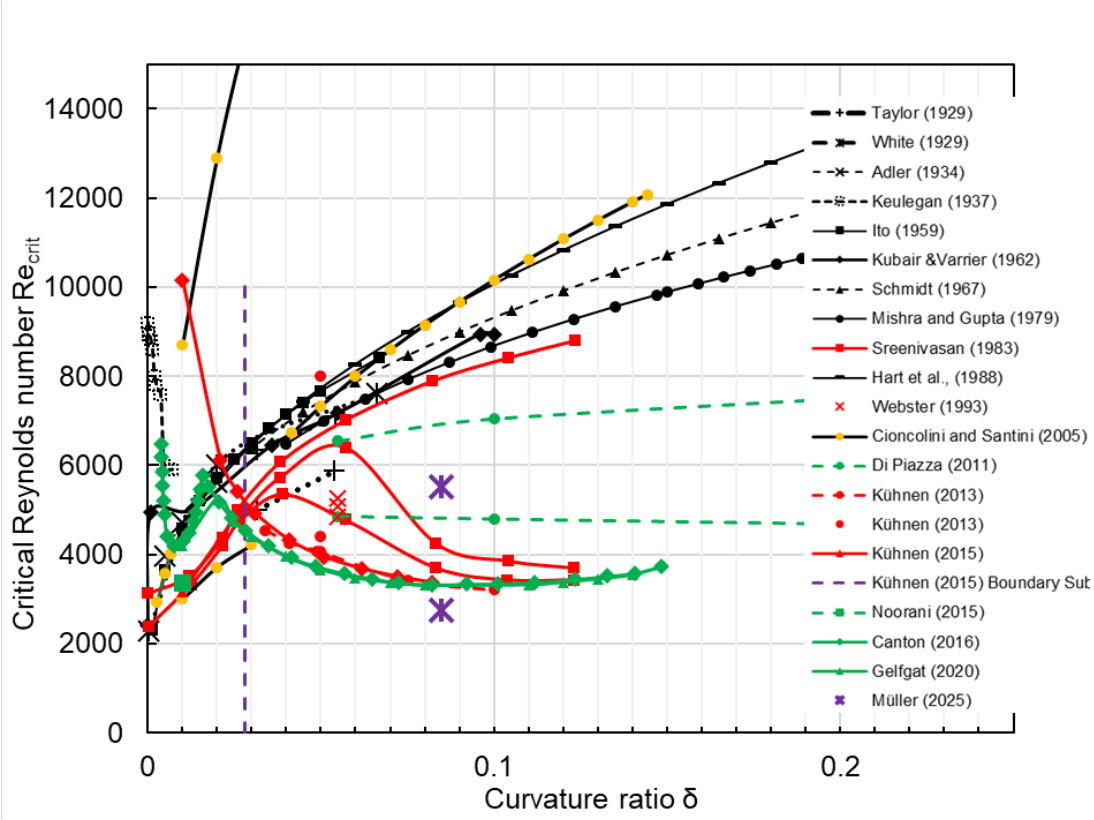

Fig. 1: All correlations from literature regarding laminar-turbulent transition in HCRs showing the critical Reynolds number in function of the curvature ratio $\delta = d/D$. Results of the present work are shown as purple crosses.

this study marked with purple crosses. They mark here a lower boundary for the first occurrence of turbulent structures (in this case first Lyne vortices), and an upper boundary (where fully-developed turbulence is achieved).

The black curves represent studies measuring the pressure drop over HCRs or curved tubes, where the transition is marked by the critical Reynolds number as function of the curvature ratio $\delta = d/D$ – i.e., the ratio of the inner diameter of the tube to the coiling diameter (Cioncolini and Santini, 2006; Hart et al., 1988; Itó, 1959; Mishra and Gupta, 1978; Schmidt, 1967). Pressure measurements show a sudden change in slope for the evolution of the friction factor as function of the Reynolds number; this is taken as an indicator of transition. The red curves represent studies measuring the velocity field in HCRs by using hot wire anemometry (HWA) (Sreenivasan and Strykowski, 1983), LDV or (stereo-) PIV (Kühnen et al., 2015, 2013). The transition in those studies is based on the velocity fluctuations in time, using either a user-prescribed threshold or a purely qualitative analysis. Quite often, studies use a 50% threshold for the time-signal of velocity, i.e., transition is assumed when noticeable fluctuations are observed during at least half of the time, with still fully laminar (steady) regions in between. For point measurements like HWA or LDV, the analysis generally concentrates on the point with the most intense fluctuations (for instance, in Kühnen et al. (2015), this position is located in a particular cross-section at $(x, y) = 0.17d, 0.31d$). More recent studies use the frequency spectrum or energy dissipation rate. The transition to turbulence is usually defined as a point with a fixed critical Reynolds number as function of the curvature ratio, this being the most important geometrical parameter. The work of Sreenivasan and Strykowski (1983) is a bit different, suggesting a transition region between a low value of the Reynolds number – corresponding to the very first occurrence of fluctuations at a point –, and a high value of Re – for which the flow is found completely turbulent in the whole cross-section of the tube.

As Fig. 1 shows, the transition point in HCRs appears to be dispersed over a very wide range, leading to a confusing picture. The differences observed between the different studies may be due to the different measurement techniques, to the specific definition of a turbulent flow, or to different geometrical parameters. Recent numerical studies (Canton et al., 2016; Gelfgat, 2020) suggest that the lower boundary (marked as solid green line in Fig. 1) should be preferred.

However, it must be kept in mind that all those studies do not involve the whole tube in the analysis. Mostly, only single points in the reactor are considered, sometimes without any clear justification for their choice. Though interesting and relevant, this local information is not sufficient to describe the full behavior of the transition process in HCRs, involving complex vortex structures – like combinations of Dean and Lyne vortices (Müller et al., 2022). Moreover, centrifugal forces lead to a completely asymmetric flow in HCRs that seems to be overlooked in many investigations.

Studies considering more simple bent tubes or a torus instead of a full helix reactor are marked with dashed lines in Fig. 1. In the torus, the flow is induced by a steel ball that is accelerated in the tube with magnets. However, this acceleration process can artificially create turbulent structures since it pushes the liquid in front. A similar effect was observed in two-phase flow studies in HCR (Müller et al., 2021) where bubbles pushed the liquid slug in front of them, inducing stable Lyne vortices.

This work establishes a measuring setup with a very high temporal and spatial resolution, paired with modern visualization approaches and analysis aiming for a highly resolved data base which is used to clarify the transition behavior and pinpoint

the actual transition point. It is an extension of the initial paper (Müller et al., 2025) with more detailed processing, improved visualizations and extensive literature research. Therefore, the measured Reynolds numbers cover the whole range of possible transition points as suggested by previous literature (Fig. 1).

2 Experimental Setup

The helix reactor employed in the present study is made of a FEP-tube (Fluorethylenepropylene) with an inner diameter of 10 mm and a coil diameter of 118 mm, resulting in a curvature ratio of $\delta = 0.0848$. In total, 50 coils are considered, resulting in a tube length of 18.53 m with additional 1 m on each side, corresponding to the straight inlet and outlet tubes. For the high-speed PIV setup, the HCR is placed in an acrylic glass tank filled with a 5.25%vol. glycerol and de-ionised water solution, which is also used as the working fluid within the helix reactor. This solution matches the refractive index of the FEP material ($n = 1.3405$), so that refraction-index matching enables very high-quality optical measurements without any reflection and refraction effects (Kováts et al., 2020). The solution has a density of $\rho = 1004.045$ kg/m^3 and a dynamic viscosity of $\mu = 0.001246$ kg m^{-1} s^{-1} (measured with a Netzsch Kinexus Pro+ rotational rheometer). Vestosint PMMA particles with a diameter of 50 µm are added to the working fluid as tracer particles. Since the density and viscosity of the 5.25 % vol. glycerol–water solution differ only marginally from those of pure water, no significant changes in the results are expected.
A feeding tank is placed 12 m above the main setup leading to a purely gravity-driven (and so pulsation-free) flow (Fig. 2). The flow rate is measured with an ultrasonic flow meter and controlled with a needle valve at the outlet of the setup. Since the flow rate must remain stable during the measurements, the liquid level in the feeding tank is controlled and kept constant using both an ultrasonic level sensor and a pressure sensor. A Phantom VEO L640 high-speed camera (2560x1600 pixels) is set in front of the tank with a 100 mm camera lens (Tokina, AT-X Pro Macro 100 F2.8D) as shown in Fig. 3.
The light source is a continuous-wave laser from Coherent (Model: Genesis MX488-1000 STM) with a 488 nm wavelength operated at 120 mW power. The geometrical calibration results in a resolution of 55 pixels/mm. Reynolds numbers (based classically on the bulk flow velocity and on the inner tube diameter) in a range of $460 < \mathrm{Re} < 9650$ are considered during the investigation. The bulk flow velocity is calculated from the volume flow rate set in the measurements and from the pipe cross-section as

$$u_b = \frac{4 \cdot \dot{V}}{\pi \cdot d_i^2} \tag{1}$$

After setting the desired flow rate, the pixel shift is kept around 2 pixels between snapshots for quantifying radial velocities. This relatively small pixel shift is necessary due to the strong out-of-plane flow movement, since the axial velocity is typically 10 times

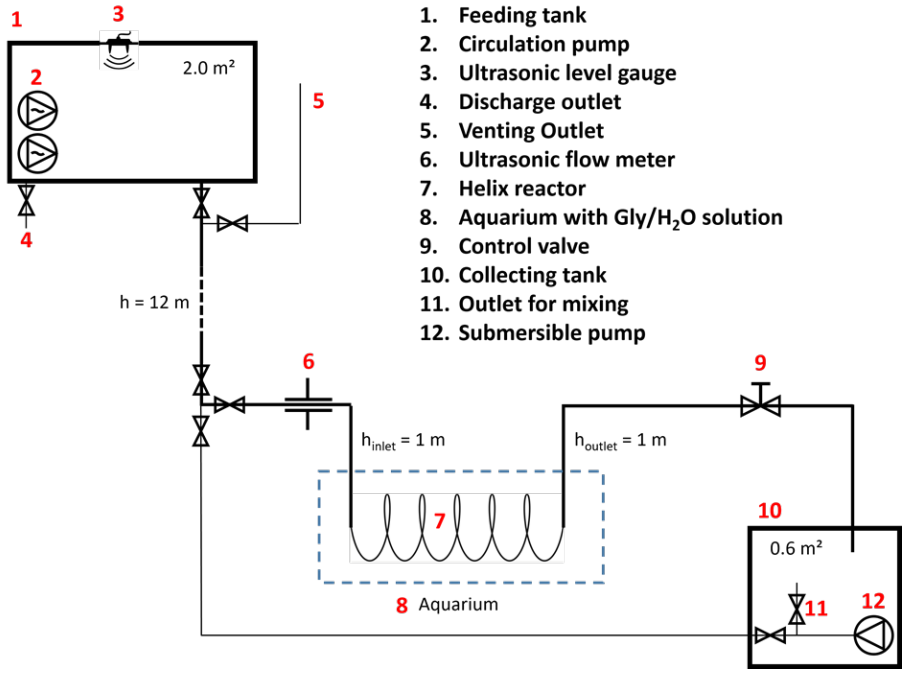

Fig. 2: Flow sketch of the experimental setup.

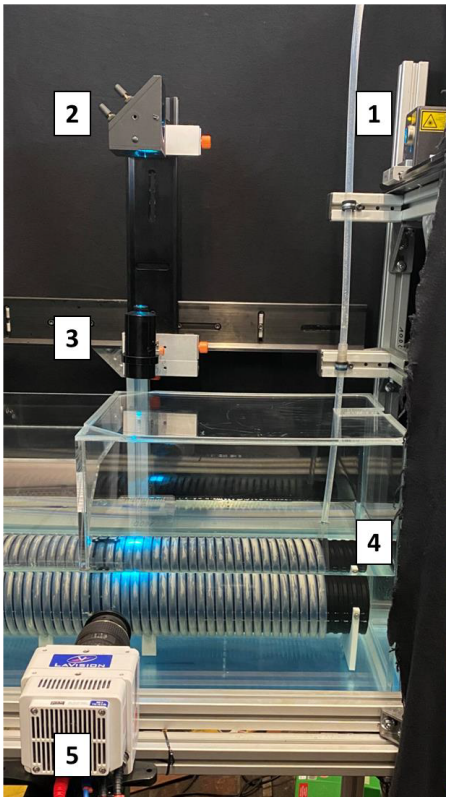

Fig. 3: Optical high-speed PIV setup with cw-laser (1), mirror (2), light sheet optics (3), aquarium with refractive index-matched solution, helix reactor (4) and HS-camera (5).

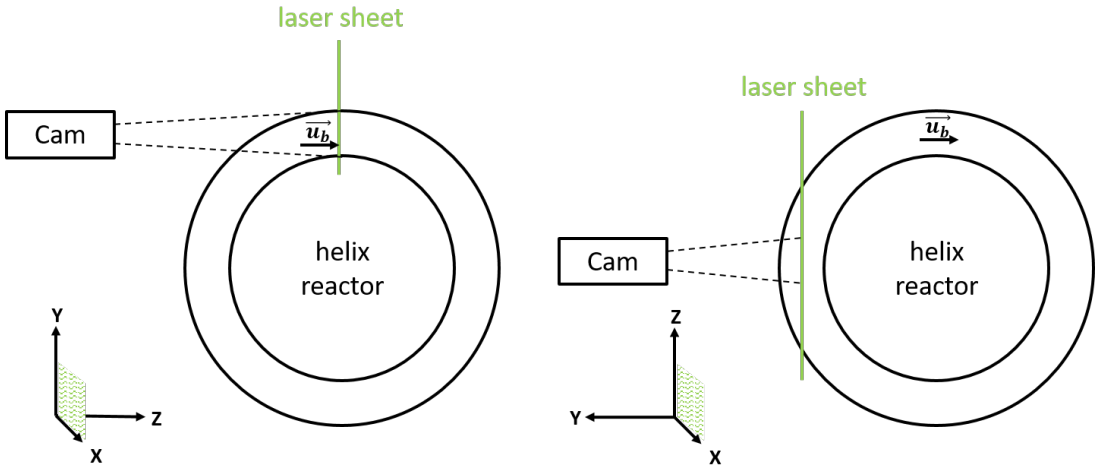

Fig. 4: Sketch of the PIV set-ups with their coordinate system and the laser light sheet in green. Left: radial velocity components. Right: axial component measured in the centre of the tube.

Tab. 1: Measurement parameters for all investigations. The acquisition frequency for the radial (penultimate column) and axial PIV measurements (last column) are also provided.

Re [−]	$\dot{V}$ [L/min]	u_b [m/s]	Q [1/s^2]	$f_{\mathrm{rec,rad}}$ [kHz]	$f_{\mathrm{rec,ax}}$ [kHz]
460	0.27	0.06	$9.85 \cdot 10^{-5}$	0.4	1.0
920	0.54	0.11	$3.94 \cdot 10^{-4}$	0.6	2.0
1370	0.80	0.17	$8.65 \cdot 10^{-4}$	0.8	3.0
2100	1.23	0.26	$2.04 \cdot 10^{-3}$	1.1	4.6
2750	1.61	0.34	$3.50 \cdot 10^{-3}$	1.4	6.0
3660	2.14	0.45	$6.19 \cdot 10^{-3}$	1.8	8.0
4580	2.68	0.57	$9.70 \cdot 10^{-3}$	2.2	10.0
5510	3.22	0.68	$1.40 \cdot 10^{-2}$	2.6	12.0
6410	3.75	0.80	$1.90 \cdot 10^{-2}$	3.0	12.0
7340	4.29	0.91	$2.49 \cdot 10^{-2}$	3.4	12.0
8240	4.82	1.02	$3.14 \cdot 10^{-2}$	3.8	12.0
9170	5.36	1.14	$3.88 \cdot 10^{-2}$	4.2	12.0
9650	5.64	1.20	$4.30 \cdot 10^{-2}$	4.5	12.0

higher compared to the radial velocities. For axial velocity measurements, a pixel shift of 5-7 pixels is considered for PIV.
For all measurements, the signal has been acquired for a physical duration of 2 s. However, different recording frequencies have been selected depending on the Reynolds number, as listed in Table 1. The axial velocity was also acquired with PIV, by measuring in the front section of the coil. For that purpose, the light sheet was set in the centre of the tube and the camera was adjusted accordingly. Figure 4 shows a sketch of both setups 1) for the radial measurements in the cross-section of the tube (left), and 2) for the axial measurements in the centre of the front part of the coil (right). The coordinate system is shown as well in this figure.
The images are then processed with DaVis 8.4 (LaVision) and the results are visualized using the open-source software ParaView 5.10. After systematic preliminary tests based on LDV (Müller et al., 2023), it was decided to acquire all measurements within the 40th coil of the HCR (from a total of 50). It was observed that the influence of both inlet and outlet vanish in this region. This has also been confirmed with axial PIV measurements (see later Fig. 7).

3 Postprocessing

The postprocessing is done in DaVis 8.4 and consists of an image calibration and a subtraction of a median Gauss filter with a filter length of 6 pixels in order to enhance the particle images. The PIV processing uses a multi-pass cross-correlation with interrogation windows of 32x32 pixels in the first 4 iteration steps, followed by 2 iteration steps with 16x16 windows with 50% overlap. The results are further postprocessed to clean-up erroneous vectors. However, only a minimum of further processing is done, keeping the vector field as raw as possible to preserve vortical and turbulent structures. Vectors with correlation values below 0.4 are removed. Finally, a median filter is applied and empty spaces are filled-up by interpolation, which is necessary for further analysis even though the amount of filled-up pixels is below 2%. For a first analysis the average vector fields with streamlines (see later Fig. 8) and the turbulence intensity based on its standard deviation are calculated and visualized to localize the first occurrence of turbulence (Fig. 9).
For this purpose, the local velocity is first extracted at 5 areas in the cross-section, marked with yellow boxes in Fig. 5 (left), and plotted in function of time. These five areas correspond to local differences of the flow, as shown by the turbulence intensity in Fig. 9. In addition, the centre velocity from the axial velocity field (yellow box in Fig. 5, right) is extracted and plotted as

well over time to visualise the fluctuations. Second, the frequency spectrum from the axial velocity is analysed based on the time plots using FFT (Fast Fourier Transformation). Third, vortex structures are reconstructed from the vector fields. For this purpose, the radial velocity fields measured in the tube cross-section are stacked along the third dimension, representing time. This third axis is normalized by dividing the bulk velocity with the recording frequency, so that the third dimension is plotted in metres. A detailed explanation how those pseudo 3D-visualizations are produced can be found in Müller et al. (2021). To analyze these three-dimensional fields, vortices are extracted using the well-known Q-criterion and plotted as isosurfaces coloured by the z-vorticity for a qualitative analysis. Since the vorticity magnitude increases with rising Reynolds number, a dimensionless Q-criterion denoted Q^* is calculated by involving characteristic length and flow velocity, resulting in:

$$Q^* = \frac{Q \cdot d_i^2}{u_b^2} = \frac{Q \cdot d_i^6 \cdot \pi^2}{16 \cdot \dot{V}^2} \tag{2}$$

All results are plotted for the same non-dimensional constant value of $Q^* = 3 \cdot 10^{-6}$ in what follows, as exemplified in Fig. 6. This non-dimensional value of Q^* (and the corresponding values of the Q-criterion shown in Table 1 in $1/s^2$) have been carefully selected during preliminary tests so that all relevant vortex structures are visible, but not overloaded with measurement noise. Note that the maximum value of Q found in the measurements is much larger but hidden inside the iso-surface of the selected Q-criterion.
Figure 6 shows a corresponding representation. The red and blue dominant vortex structures delineate the well-known Dean vortices in the helix reactor. Additional vortex structures (Lyne vortices) appear first and mainly in the top part of the tube, since the velocity in this outer region is higher due to the radial forces pushing the liquid to the outer side of the tube. For a better comparison, those pseudo-3D-visualizations are shown in the next section (see later Fig. 14) with a view from the top, with the Dean vortices appearing as continuous lines on both sides of the tube while additional vortex structures are occasionally observed in-between.

4 Results

In order to check first the independency of the measurement position from perturbations coming with inlet and outlet conditions, the axial velocity has been systematically measured in each coil. It has then been analyzed by plotting velocity over time at the

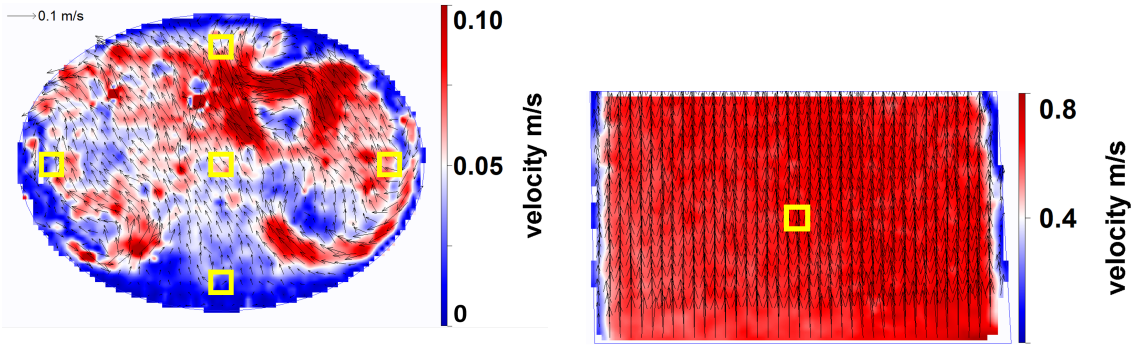

Fig. 5: Exemplary instantaneous flow fields in the 40th coil (Re = 3660) showing the radial vector field (left) and the axial vector field (right) with the velicity magnitude as background colour. The selected extraction regions at which the evolution of local velocity over time will be tracked and analyzed are marked in yellow.

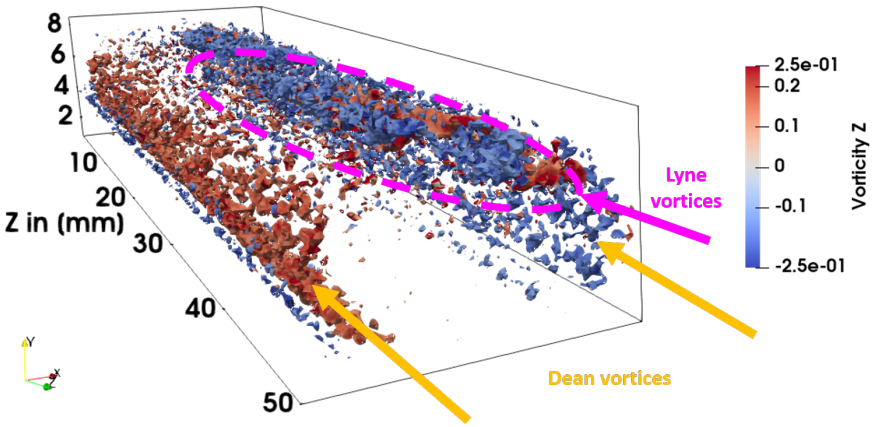

Fig. 6: Pseudo-3D-visualization of vortical structures for Re = 2750. The field of Q^* is shown as an iso-surface equal to $3 \cdot 10^{-6}$ and coloured by the z-vorticity. The y-direction is the vertical direction, with gravity pointing towards negative y. Dean vortices are exemplarily marked with yellow arrows, Lyne vortices with a pink arrow.

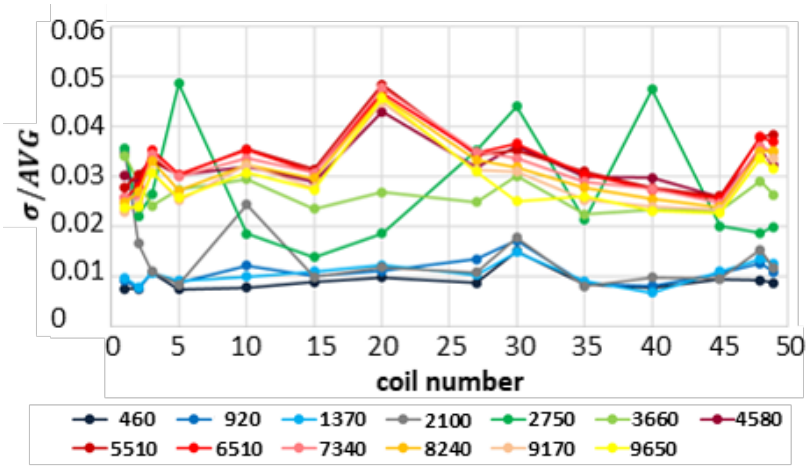

Fig. 7: Normalized standard deviation of axial velocity as function of Reynolds number depending on the coil number, from straight inlet (ending at position #0) to straight outlet (starting at position #50), Müller et al. (2025).

centre position (yellow square in Fig. 5, right) and computing its standard deviation normalized by the average velocity as function of the coil number, as shown in Fig. 7.

After the first 3 coils, where the initial straight tube flow gets transformed into a flow dominated by radial acceleration, the standard deviation progressively stabilizes due to the re-laminarizing effect induced by the very stable, secondary flow controlled by the Dean vortices. However, this stabilization process needs up to 30 (sometimes even 40) coils before reaching a final state. This is especially true at intermediate Reynolds numbers (Re = 2750 and 3660). The impact of the outlet boundary condition is also clearly noticeable with a sudden increase of the standard deviation for the last 2 to 3 coils. This shows that 1) the first and last 3 coils should be excluded from the analysis, and 2) a long reactor is necessary, the measurements ideally taking place after 40 coils – as done in the present investigation.

The normalized standard deviation (also known as turbulence intensity) of the axial velocity sorts itself into two separate regions. In Fig. 7, low Reynolds numbers up to Re = 2100 have a turbulence intensity around 1% (blue/grey curves). Reynolds numbers higher than Re = 4580 (yellow and red curves) come with a turbulence intensity three to four times higher, up to almost 5% locally. Kühnen et al. (2015) described this noticeable increase in standard deviation as one indicator for the laminar-turbulent transition. A transition area can be noticed for the Reynolds numbers between Re = 2750 and 3660: the two corresponding (green) curves behave quite differently, connecting the two regions discussed previously.

Figure 8 shows the streamline visualization based on the average flow fields for different Reynolds numbers. Easily detectable are the two vortex cores of the steadily occurring Dean vortices. Remarkable is, that even for higher Reynolds numbers, those average flow fields only show the Dean vortices as dominant structures. By contrast, Fig. 9 reveals the change of the flow with increasing Reynolds number when plotting turbulence intensity. In the laminar case (Re = 460) the turbulence intensity is low with peaks close to the wall and areas of higher values connected to the Dean vortices. At Re = 2750, the turbulence intensity in the top part of the helix cross-section jumps drastically due to the onset of Lyne vortices. Over the range of Re = 3660 ... 9650 the area corresponding to a high turbulence intensity progressively increases in the cross-section from top to bottom, stretching even into the lowest part of the tube, where averaged turbulence intensities of TI > 50% are reached. Noticeable is also a local peak at the bottom where Dean vortices are observed to start interacting for Re = 9650. This reveals a highly non-homogeneous evolution, with strong local differences regarding the occurrence of turbulence in helix reactors.

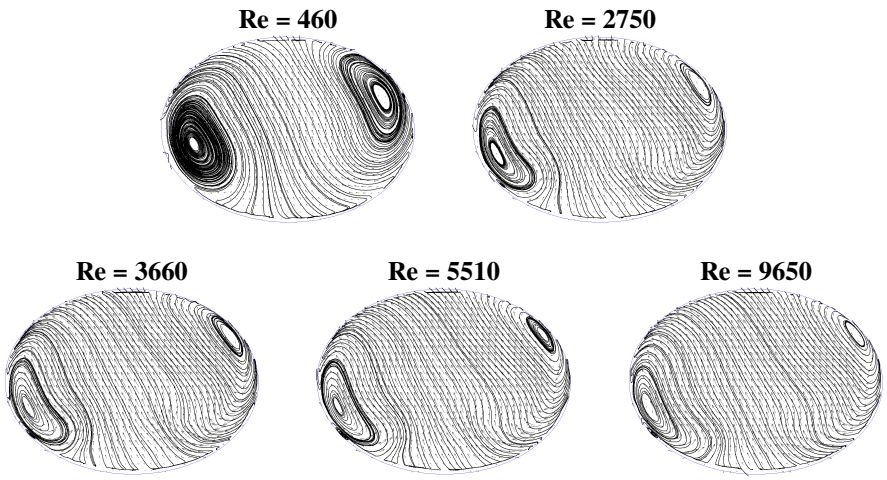

Fig. 8: Streamline visualization of averaged flow fields in the cross-section of the helix for different Reynolds numbers.

Tab. 2: Frequencies f_1 and f_2 with the highest amplitude for different Reynolds numbers.

Re [−]	f_1 [Hz]	f_2 [Hz]
460	–	–
2750	1	3
3660	6	36
5510	7	22

Figure 10 shows the velocity in function of time for the 5 points shown in the yellow boxes in Fig. 5 (left). From these plots it is obvious, that with rising Reynolds number the fluctuations of the flow become systematically stronger, as expected. However, there are also clear differences depending on the specific location within the cross-section of the coil. While the fluctuations already start to be strong at Re = 5510 in the top position, as well as on the left and right side (where the Dean vortices are situated), they are much less pronounced in the centre, and stay almost negligible at the bottom location for this same Reynolds number.
The evolutions of axial velocities over time in Fig. 11 show a similar trend, with an increase of fluctuations with rising Reynolds number. When taking a look onto a full measurement period (Fig. 12), not only high-frequency fluctuations but also oscillations at lower frequencies become visible; a more detailed investigation of these different contributions is left for future work.
Figure 13 shows the frequency spectra of the axial velocity measurements for selected Reynolds numbers. As expected, in a completely laminar flow (Re = 460) no frequency could be detected. At intermediate Reynolds numbers, individual frequencies become pronounced. The two frequencies with the highest amplitude are listed in Table 2. Increasing further the Reynolds number, the frequency spectrum broadens until a full range of frequencies is observed.
For a more detailed analysis of the flow it seems reasonable to visualize the flow as a whole. The instantaneous flow fields are therefore extended to pseudo-3D-visualizations, as explained previously. Figure 14 shows the results for a selection of Reynolds numbers. The view is from the top, looking down through the helix tube, and the flow goes from left to right. The vortex structures are visualized using the non-dimensional Q^*-criterion, coloured with z-vorticity component. The represented pseudo-distance of 100 mm contains around 500 images (this number varies slightly depending on the recording frequency and bulk velocity). At low Reynolds numbers, the counter-rotating Dean vortices are clearly visible as horizontal stripes near the tube walls, indicating a stable and laminar flow. With increasing Reynolds number, Lyne vortices first occur near the centre of the cross-section. They merge at some time with the Dean vortices on either side (see the black ellipse in Fig. 14 for an example of such an event for Re = 2750) and temporarily disappear, indicating first instabilities and transition to turbulence. For even faster flows (for instance for Re = 3660) the Lyne vortices appear and disappear with a higher frequency. At an even higher Reynolds number the Lyne vortices are no longer distinguishable and the whole flow becomes turbulent; even the Dean vortices are so smeared that they cannot be identified clearly, indicating a turbulent flow behavior (Fig. 14, Re = 5510). At the highest measured flow rate, with a Reynolds number of Re = 9650, the vortex structures have a comparable intensity, size, and lifetime. It has to be noted, that with increasing Reynolds number the overall vorticity magnitude also increases.

5 Conclusions

In this study, the laminar-turbulent transition in helical coils has been examined based on LDV and PIV measurements. The independence from inlet and outlet conditions was obtained in the region around coil #40 for a reactor involving a total of 50

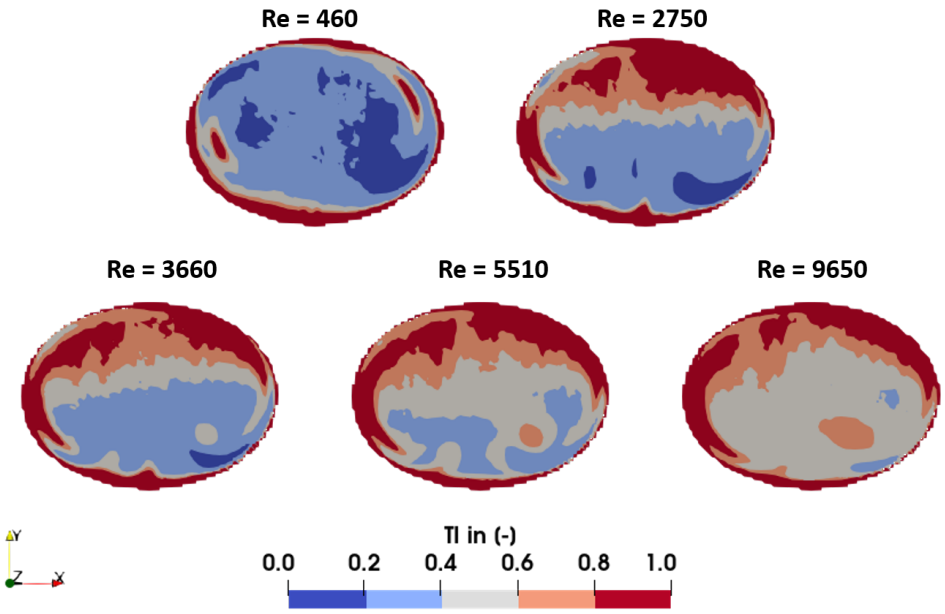

Fig. 9: Turbulence intensity of averaged flow fields in the cross-section of the helix for different Reynolds numbers.

coils. The qualitative analysis of the velocities, measured in the 40th coil, confirms the findings of Sreenivasan and Strykowski (1983): there is both a lower boundary in terms of Reynolds number, corresponding to the onset of turbulence at a specific location within the coil cross-section, and an upper boundary corresponding to fully-developed turbulence within the whole cross-section. Depending on the location in the cross-section of the helix, the flow behaves very differently. While in the outer region of the HCR (here, the top of the cross-section), strong fluctuations appear at a much lower Reynolds numbers (Re = 5510), the onset of turbulence in the inner region (here, the bottom of the cross-section) is only observed at the highest measured Reynolds number of Re = 9650. The FFT analysis of the axial velocities did not show detectable frequencies for laminar flow conditions. In the transition area characteristic frequency peaks appear, and a broadening of the frequency spectrum is observed when reaching the turbulent region. While the spectra delineate laminar from turbulent flows, the frequencies alone are not able to show a clear difference between the transitional and the turbulent regime. Pseudo-3D-visualizations of vortical structures derived from the radial velocities show first high-order structures appearing as Lyne vortices at a Reynolds number Re = 2750 and a turbulent flow behavior at Re = 5510. This range then covers the transition range between the laminar and fully turbulent flow conditions which is marked in Fig. 1 with two purple crosses for the lower and upper boundary, respectively. The proposed pseudo-3D-visualization provides a more revealing view of the vortex behavior in the helical reactor by combining a time-resolved and a spatially-resolved analysis.

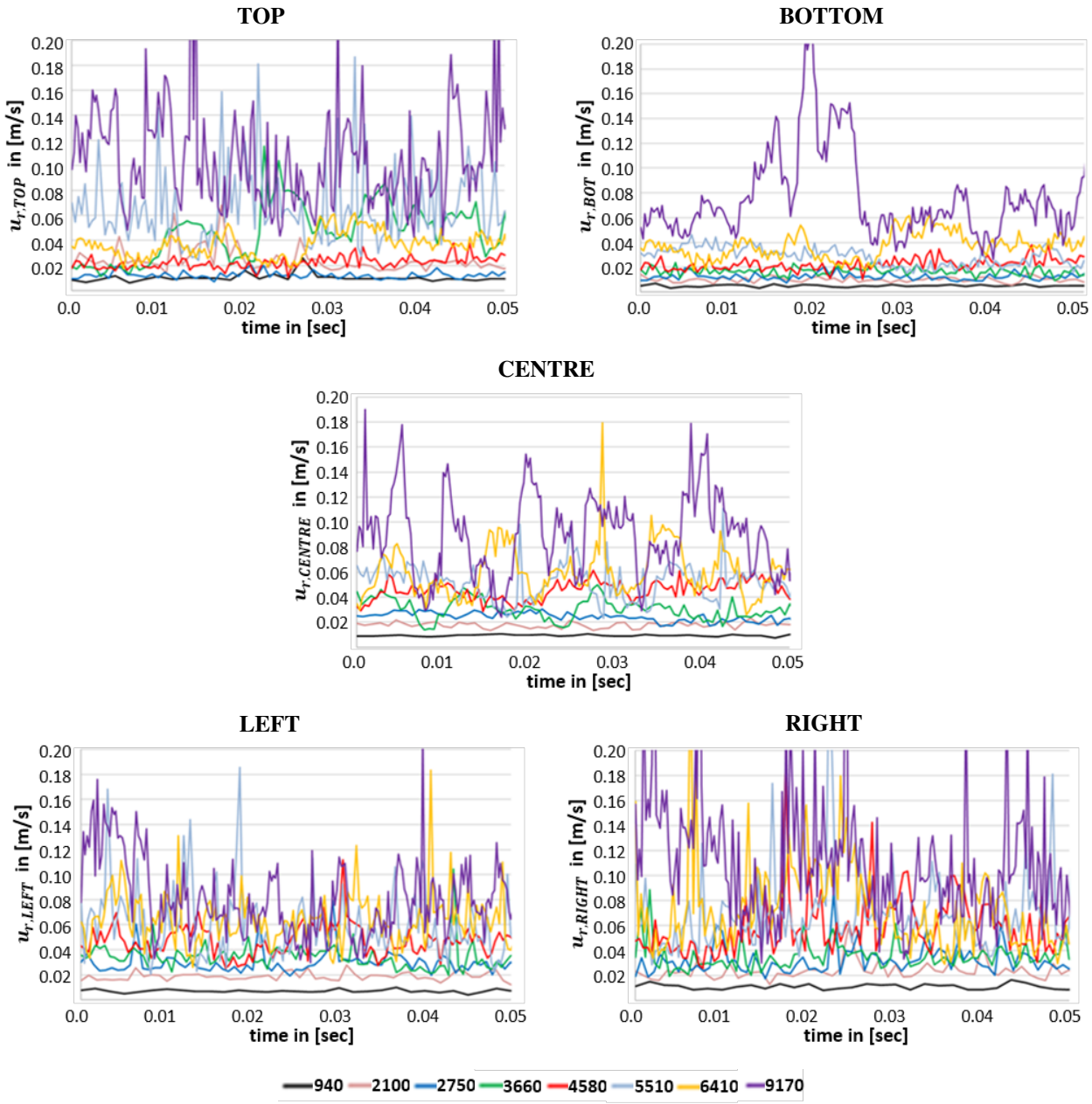

Fig. 10: Extracted radial velocity over time for different Reynolds numbers. Locations of the yellow squares shown in Fig. 5 (left) from top to bottom and left to right: Top, Bottom, Centre, Left, Right (as marked on the subfigures), Müller et al. (2025).

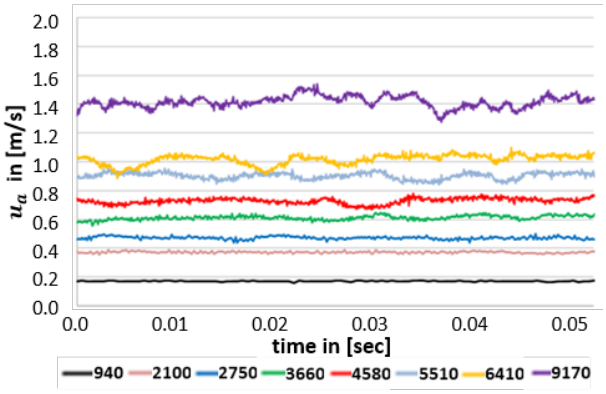

Fig. 11: Extracted axial velocity over time for different Reynolds numbers, Müller et al. (2025).

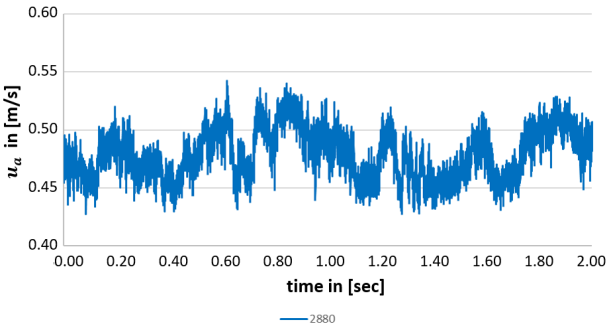

Fig. 12: Extracted axial velocity over time for a Reynolds number of 2750 and for the whole measurement time of 2 s. Note the different vertical scale compared to Figure. 11, Müller et al. (2025).

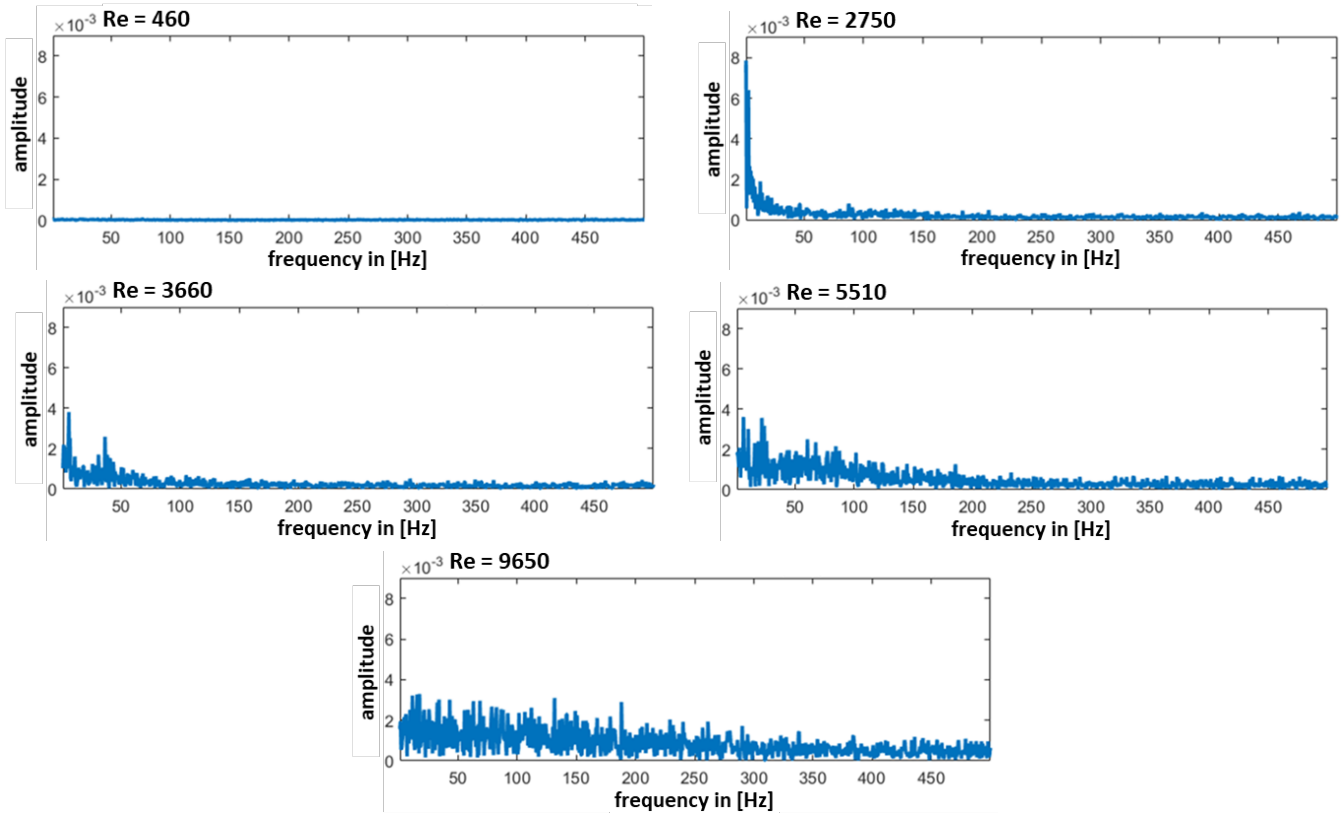

Fig. 13: FFT analysis of the axial velocity for different Reynolds numbers, Müller et al. (2025).

6 Outlook

While searching for the laminar-turbulent transition point in HCRs it becomes clear, that in such an asymmetric flow the results depend strongly on the particular location selected. The markers of transition discussed here are either focused on one point in the flow or are mostly qualitative. For a quantitative analysis, measurements at high spatial and temporal resolution are necessary to capture the vortex structures with a high accuracy and low measurement noise. A combination of markers will help to capture all flavours of turbulence, supporting the difference between stable or frequent structures like Lyne vortices and fully turbulent, chaotic vortical structures. A holistic view of all markers is necessary for cross-validation but also to make a final decision regarding the transition point. In addition, the asymmetric flow profile in radial direction leads to high velocities in the outer regions compared to regions closer to the core of the helix reactor. The Reynolds number is normally calculated based on the bulk flow velocity and thus from the volume flow rate. Defining a local Reynolds number based on the local axial flow velocity could lead to a more consistent definition of the transition point comparing the inner and outer regions in the tube. However, for real-world applications, keeping a single global value for the critical Reynolds number would be far more practicable.

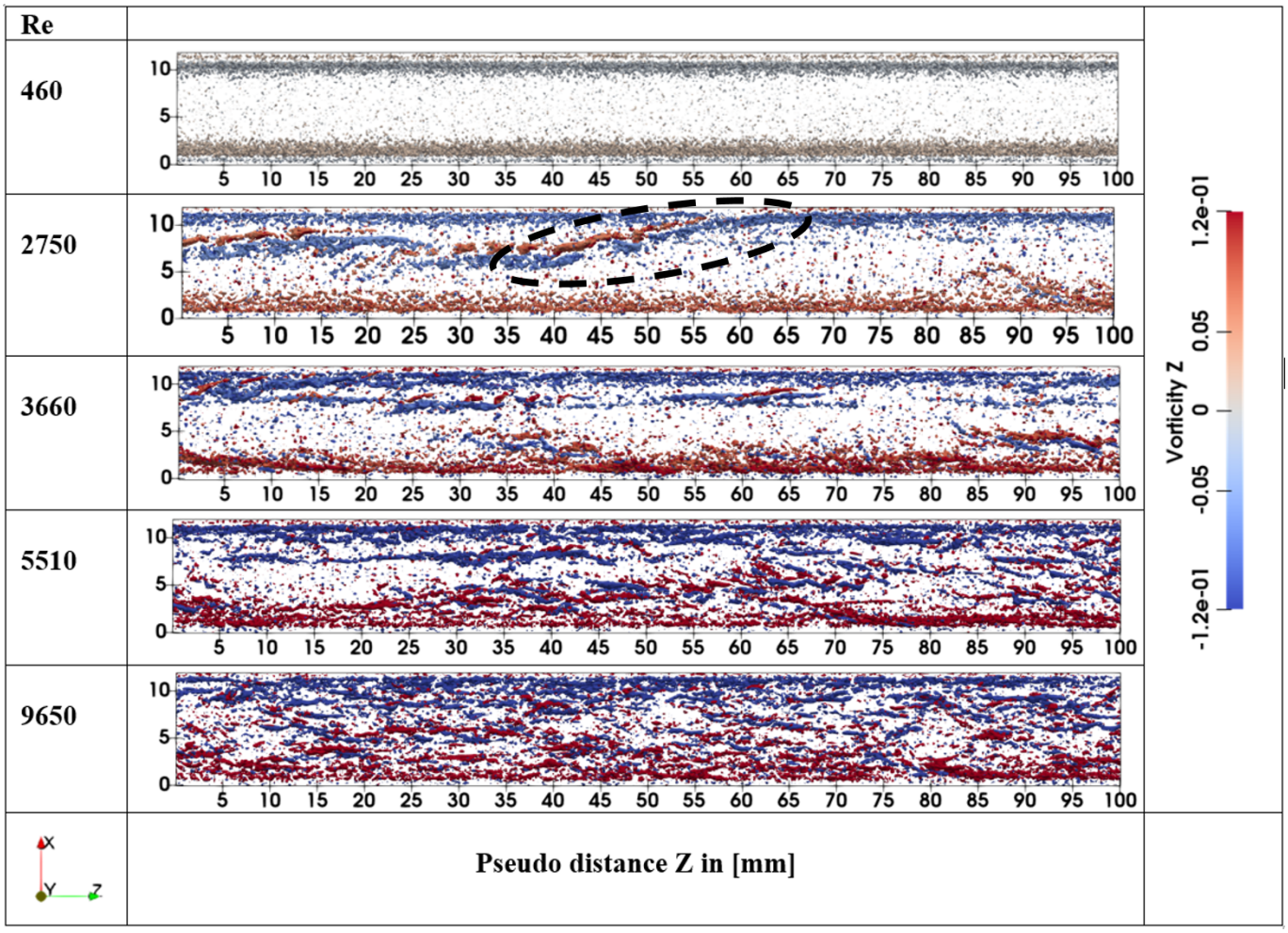

Fig. 14: Pseudo-3D-visualizations of the vortex structures derived from radial velocity fields and revealed by the non-dimensional Q-criterion ($Q^* = 3 \cdot 10^{-6}$) colored by z-vorticity component. The view is from top to bottom through the coil.

Acknowledgments

The PIV measurement system employed for this study has been funded by the Deutsche Forschungsgemeinschaft (DFG, German Research Foundation) under project number 444994527. The authors would like to thank Justus Herzig for his help and support in carrying out the measurements.

References

M. Adler. Strömung in gekrümmten Rohren. *ZAMM - Journal of Applied Mathematics and Mechanics / Zeitschrift für Angewandte Mathematik und Mechanik*, 14(5):257–275, 1934. ISSN 0044-2267 1521-4001. doi: 10.1002/zamm.19340140502.

S. Ali. Pressure drop correlations for flow through regular helical coil tubes. *Fluid Dynamics Research*, 28:295–310, 2001.

J. Canton, P. Schlatter, and R. Örlü. Modal instability of the flow in a toroidal pipe. *Journal of Fluid Mechanics*, 792:894–909, 2016. ISSN 0022-1120 1469-7645. doi: 10.1017/jfm.2016.104.

A. Cioncolini and L. Santini. An experimental investigation regarding the laminar to turbulent flow transition in helically coiled pipes. *Experimental Thermal and Fluid Science*, 30(4):367–380, 2006. ISSN 08941777. doi: 10.1016/j.expthermflusci.2005.08.005.

S. K. Das. *Water flow through helical coils in turbulent conditions*, pages 379–403. 1996. doi: doi.org/10.1016/B978-088415497-6/50015-2.

F. Florit, R. Rota, and K. F. Jensen. Dispersion in coiled tubular reactors: A CFD and experimental analysis on the effect of pitch. *Chemical Engineering Science*, 233, 2021. ISSN 00092509. doi: 10.1016/j.ces.2020.116393.

A. Y. Gelfgat. A comparative study on instability of steady flows in helical pipes. *Fluid Dynamics Research*, 52(1), 2020. ISSN 1873-7005. doi: 10.1088/1873-7005/ab6618.

J. Hart, J. Ellenberger, and P. J. Hamersma. Single and two phase flow through helically coiled tubes. *Chemical Engineering Science*, 43:775–783, 1988.

T. J. Hüttl and R. Friedrich. Influence of curvature and torsion on turbulent flow in helically coiled pipes. *International Journal of Heat and Fluid Flow*, 21:345–353, 2000.

H. Itó. Friction factors for turbulent flow in curved pipes. *Journal of Basic Engineering*, pages 123–132, 1959.

G. H. Keulegan and K. H. Beij. Pressure losses for fluid flow in curved pipes. *Journal of Research of the National Bureau of Standards*, 18:90–114, 1937.

N. Kockmann. Entwurf und Betrieb eines Rohrreaktors mit enger Verweilzeitverteilung. *Chemie Ingenieur Technik*, 92(6):685–691, 2020. doi: 10.1002/cite.202000028.

P. Kováts, C. Velten, M. Mansour, D. Thévenin, and K. Zähringer. Mixing characterization in different helically coiled configurations by laser-induced fluorescence. *Experiments in Fluids*, 61(9), 2020. doi: 10.1007/s00348-020-03035-0.

V. Kubair and C. B. S. Varrier. Pressure drop for liquid flow in helical coils. *Transactions of the Indian Institute of Chemical Engineers*, pages 93–97, 1962.

J. Kühnen, M. Holzner, B. Hof, and H. C. Kuhlmann. Experimental investigation of transitional flow in a toroidal pipe. *Journal of Fluid Mechanics*, 738:463–491, 2013. ISSN 0022-1120 1469-7645. doi: 10.1017/jfm.2013.603.

J. Kühnen, P. Braunshier, M. Schwegel, H. C. Kuhlmann, and B. Hof. Subcritical versus supercritical transition to turbulence in curved pipes. *Journal of Fluid Mechanics*, 770, 2015. ISSN 0022-1120 1469-7645. doi: 10.1017/jfm.2015.184.

S. Liu, A. Afacan, H. A. Nasr-el Din, and J. H. Masliyah. An experimental study of pressure drop in helical pipes. *Proceedings of the Royal Society A: Mathematical, Physical and Engineering Sciences*, 444:307–316, 1994.

R. L. Manlapaz and S. W. Churchill. Fully developed laminar flow in a helically coiled tube of finite pitch. *Chemical Engineering Communications*, 7(1-3):57–78, 1980. ISSN 0098-6445 1563-5201. doi: 10.1080/00986448008912549.

M. Mansour and D. Thévenin. Mixing device with reversed coiled configuration and use thereof. *Patent*, (19176360.6), 2023. ISSN EP19176360NWB1.

P. Mishra and S. N. Gupta. Momentum transfer in curved pipes 1. Newtonian fluids. *Industrial & Engineering Chemistry Process Design and Development*, 18, 1978.

C. Müller, P. Kováts, and K. Zähringer. Experimental characterization of mixing and flow field in the liquid plugs of gas–liquid flow in a helically coiled reactor. *Experiments in Fluids*, 62(9), 2021. ISSN 0723-4864 1432-1114. doi: 10.1007/s00348-021-03284-7.

C. Müller, P. Kováts, and K. Zähringer. On the existence, formation and stabilization of Lyne vortices in helically coiled reactors at moderate Reynolds numbers. In *20th International Symposium on the Application of Laser and Imaging Techniques to Fluid Mechanics (LXLASER'22)*, 2022.

C. Müller, P. Kováts, and K. Zähringer. Experimental investigation of the laminar-turbulent transition in helically coiled reactors with LDA. In *Fachtagung "Experimentelle Strömungsmechanik" (GALA'23)*, 2023.

C. Müller, P. Kováts, D. Thévenin, and K. Zähringer. Laminar - turbulent transition in helically coiled reactors. an experimental study with high-speed PIV. In *19th International Conference on Fluid Flow Technologies CMFF'25, (Vad, J., Ed.), Budapest, Hungary*, pages 43–50, 2025.

A. Noorani and P. Schlatter. Evidence of sublaminar drag naturally occurring in a curved pipe. *Physics of Fluids*, 27(3), 2015. ISSN 1070-6631 1089-7666. doi: 10.1063/1.4913850.

I. D. Piazza and M. Ciofalo. Transition to turbulence in toroidal pipes. *Journal of Fluid Mechanics*, 687:72–117, 2011. ISSN 0022-1120 1469-7645. doi: 10.1017/jfm.2011.321.

E. F. Schmidt. Warmeübergang und Druckverlust in Rohrschlangen. *Zeitschrift fur Technische Chemie, Verfahrenstechnik und Apparatewesen*, 39:781–832, 1967.

K. R. Sreenivasan and P. J. Strykowski. Stabilization effects in flow through helically coiled pipes. *Experiments in Fluids*, 1:31–36, 1983.

G. I. Taylor. The criterion for turbulence in curved pipes. *Royal Society Publishing*, 1929.

D. R. Webster and J. A. C. Humphrey. Experimental observations of flow instability in a helical coil (data bank contribution). *Journal of Fluids Engineering*, 115:436–443, 1993.

C. M. White. Streamline flow through curved pipes. *Proceedings of the Royal Society of London. Series A, Containing Papers of a Mathematical and Physical Character*, 123(792):645–663, 1929.

D. G. Xie. Torsion effect on secondary flow in helical pipe. *International Journal of Heat and Fluid Flow*, 11, 1990.